Available online at www.sciencedirect.com
SCIENCE DIRECT
Electrochimica Acta 51 (2006) 3658–3667
ELECTROCHIMICA Acta
www.elsevier.com/locate/electacta

Electrochemical activation and electrocatalytic enhancement of a hydride-forming metal alloy modified with palladium, platinum and nickel

A. Visintin [a,*], E.B. Castro [a], S.G. Real [a], W.E. Triaca [a,1], C. Wang [b], M.P. Soriaga [c]

[a] *Instituto de Investigaciones Fisicoquímicas, Teóricas y Aplicadas, Universidad Nacional de La Plata, La Plata, Argentina*
[b] *Department of Chemical Engineering, Tennessee Technological University, Cookeville, TN 38505, USA*
[c] *Department of Chemistry, Texas A&M University, College Station, TX 77843, USA*

Received 6 June 2005; received in revised form 26 August 2005; accepted 15 October 2005
Available online 29 November 2005

Abstract

The influence of the addition of polycrystalline Pt, Pd and Ni powders into hydride-forming metal alloy electrodes on the activation process, rate-capability and cycling stability has been evaluated. The metal powder additives were found to improve the activation rate and to decreased the overpotentials of the charge and discharge processes. The electrochemical properties of these modified electrodes were analysed in terms of a simplified form of a previously developed model. Electrochemical impedance spectroscopy measurements were performed to allow the validation of the model and the identification of kinetic and physicochemical parameters.

Keywords: Metal hydride electrodes; Hydrogen; Electrochemical impedance spectroscopy; Porous electrodes; Alkaline rechargeable batteries

1. Introduction

Metal hydride (MH_x) electrode materials used for Ni-metal hydride (Ni-MH_x) secondary batteries continue to be extensively studied due to their high capacity, high rate-capability, long cycling life and environmental compatibility [1–4]. Among the hydride-forming materials, the AB_5-type alloys have been successfully commercialised for Ni-MH batteries due to their excellent electrochemical performance. Moreover, multicomponent and multiphase AB_2-type alloys, although slightly slower to get activated, have been regarded as viable candidates to comply with the above requirements due to their large hydrogen-storage capacity. This has given rise to extensive work in recent years, aiming to understand the roles of both alloy composition and microstructure and their correlation with solid–gas and electrochemical reactions [5–9].

The activation of the metal alloy plays a key role in the electrode absorption/desorption process, since it defines the rate of the reaction of hydrogen with the metal and the incorporation of hydrogen into the bulk structure of the metal. During activation, several different processes occur [10–14] such as: (i) reduction of surface oxides that interfere with hydrogen, (ii) reduction of particle size due to cracks induced by the volume changes, (iii) changes in the chemical composition and/or surface structure of the metal, (iv) protonation of the surface oxide, increasing the conductivity of the alloy particles.

It is well known that Pt, Pd and Ni are excellent catalysts for the electrochemical hydrogen reaction and become very stable in alkaline solution. For AB_5-type alloys, it has been demonstrated that the presence of amorphous-Pd-coatings improves the cycle lifetime and high-rate discharge ability of metal hydride electrodes [15]. Since hydrogen absorption on amorphous-Pd powder is negligible [16], the enhancement in the electrode performance has been explained on the basis of the electrocatalytic effect of Pd-coating on the kinetics of the charge transfer process at the electrode surface, which is the rate determining step in the overall hydriding/dehydriding processes [15–17].

In this paper, the effect of the addition of polycrystalline Pd, Pt and Ni powders into hydride-forming metal alloy electrodes on the activation, rate-capability and cycling stability was investigated employing charge–discharge techniques and electrochem-

* Corresponding author.
E-mail address: avisintin@inifta.unlp.edu.ar (A. Visintin).
[1] ISE member.

0013-4686/$ – see front matter © 2005 Elsevier Ltd. All rights reserved.
doi:10.1016/j.electacta.2005.10.019

ical impedance spectroscopy (EIS). The EIS data were analysed using a modification of the model developed by the authors [18].

2. Experimental details

AB_5-type alloys with nominal composition of $MmNi_{4.1}Co_{0.4}Mn_{0.4}Al_{0.5}$, where Mm (mishmetal) is 43% La, 3.5% Ce, 13.3% Pr and 38.9% Nd, 200 mesh size from Japan Metals & Chemical Co. Ltd. were used as hydride-forming metal alloys. To prepare hydride-forming electrodes, the Mm-based alloy was first mixed with different amounts of Pt, Pd, or Ni powder and 50 wt.% of teflonised carbon black (Vulcan-XC-72, with 33 wt.% PTFE). The mixture was then pressed onto a nickel mesh under a pressure of 3500 kg/cm^2 at room temperature. The geometric area of the electrodes was 2 cm^2 and the thickness was around 1 mm. The amount of active material (i.e., alloy powder) used per electrode was 75 mg.

Electrochemical measurements were made in a three-compartment cell with the corresponding working electrode (metal hydride electrode), counter electrode (sintered NiOOH), and reference electrode (Hg/HgO electrode). The electrolyte, 7 M KOH solution, was prepared from reagent grade KOH and deionized water. The experiments were carried out at 25 °C. The electrochemical capacities were measured by charging the working electrodes with a current of C/2 mA for 2 h 50 min and subsequently discharging them at C/2 up to the cut off potential of −0.6 V versus Hg/HgO. The rate capabilities of the different alloy electrodes were determined at discharge currents between 1 and 100 mA, after a previous charge under the above-mentioned conditions. The EIS measurements were conducted over a frequency range from 65 kHz to 0.01 Hz at equilibrium conditions with a superimposed sinusoidal voltage signal of 10 mV amplitude, using a frequency response analyser Solartron FRA 1250 and an electrochemical interface Solartron model 1286.

3. Results and discussion

3.1. Activation and charge–discharge stability of hydride-forming metal alloy electrodes

Fig. 1 shows the discharge capacities of the Mm-based alloy electrodes with different amounts of Ni powder during charge–discharge cycles at C/2 rates. The capacities of all electrodes first increased with charge–discharge cycles, and then begin to decrease after reaching the maximum capacity of about 250 mAh/g. More than 50 charge–discharge cycles are needed for metal alloy electrodes to reach their maximum capacity, while only 10 cycles are needed for Ni-additivated alloy electrodes activation. The electrode capacity changes in Fig. 1 suggest that Ni addition into metal alloy electrode really accelerates the activation process of the electrodes. The decrease in the electrode capacity after ca. 150 charge–discharge cycles may be attributed to pulverization and corrosion of metal alloy particles in alkaline media due to crack formation during the hydriding/dehydriding processes [3], this effect being more significant for alloy electrodes with 20 wt.% Ni content subjected to relatively larger volume changes. The alloy electrodes with 5–10 wt.% of Ni exhibit the best performance.

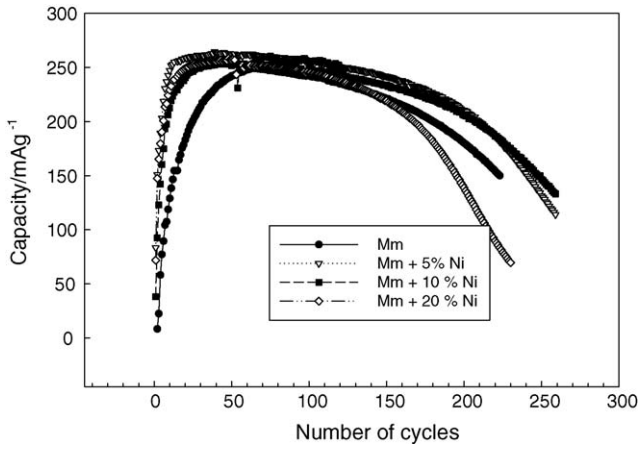

Fig. 1. Capacities of the Mm-based alloy electrodes with different Ni powder content as a function of the number of charge–discharge cycles at C/2 rates; 7 M KOH, 23 °C.

The addition of Pd powder not only drastically enhanced the activation process of the metal alloy electrode, but also increased the electrode capacity as shown in Fig. 2(a). The maximum elec-

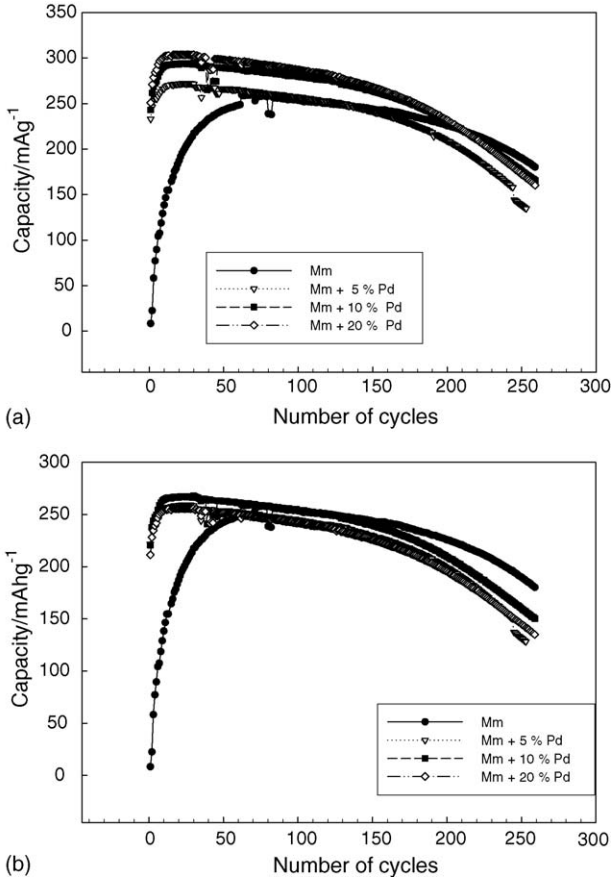

Fig. 2. Capacities of the Mm-based alloy electrodes with different Pd powder content as a function of the number of charge–discharge cycles at C/2 rates; 7 M KOH, 23 °C: (a) capacities values referred to Mm–based alloy weight; (b) capacities values referred to the total weight of catalyst plus to Mm–based alloy.

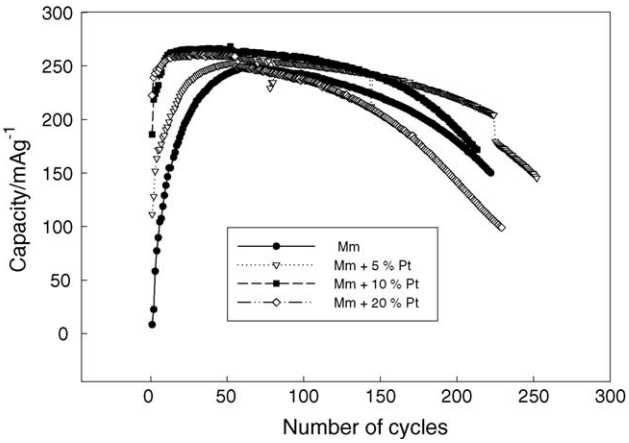

Fig. 3. Capacity of the Mm-based alloy electrodes with different Pt powder content as a function of the number of charge–discharge cycles at C/2 rates; 7 M KOH, 23 °C.

trode capacity increases with the addition of Pd powder because this metal can absorb hydrogen to form a metal hydride, namely, $PdH_{0.7}$. As Pd polycrystalline becomes also an active material for hydrogen absorption, in Fig. 2(b), for the sake of comparison with other metal catalysts, the capacity values are referred to the total weight of catalyst plus alloy. In this case, as can be expected, the full capacity remains approximately constant, on electrode Pd content, since the increase in active material weight is compensated by the hydrogen absorption ability of Pd. The capacity gradually decreased with charge–discharge cycles, the decrease became faster after 150 cycles.

The addition of Pt powder, similarly to Ni and Pd, largely accelerate the activation process of the metal alloy electrode. However, Pt addition did not increase significantly the capacity of the metal alloy (Fig. 3), which remained similar to that of electrodes with Ni additive. Alloy electrodes with 10 wt.% Pt attained the full capacity after 2–5 cycles. The electrode capacity decreased slightly under cycling, but after 250 cycles it falls significantly. In this case, the best performance corresponds to the alloy with 5 wt.% Pt addition.

As can be inferred from Figs. 1–3, the metal powder addition largely accelerates the activation process, but it does not enhance the cycling stability of metal hydride electrodes. The effectiveness of metal powder addition to accelerate activation decreased in the following order of Pt > Pd, Ni.

3.2. Effect of metal catalyst addition on charging–discharging overpotentials of metal hydride electrodes

To investigate the effect of metal catalyst addition on the overpotentials related to the hydriding/dehydriding processes, the charge–discharge profiles of alloy electrodes with different metal catalyst content were analysed. In Fig. 4, the potential changes during charging and discharging cycles corresponding to metal alloy electrodes with different Pt powder content are depicted. During the first charge–discharge cycle (Fig. 4a), the metal hydride electrode without metal catalyst addition, shows a high charge overpotential and a low capacity. Furthermore,

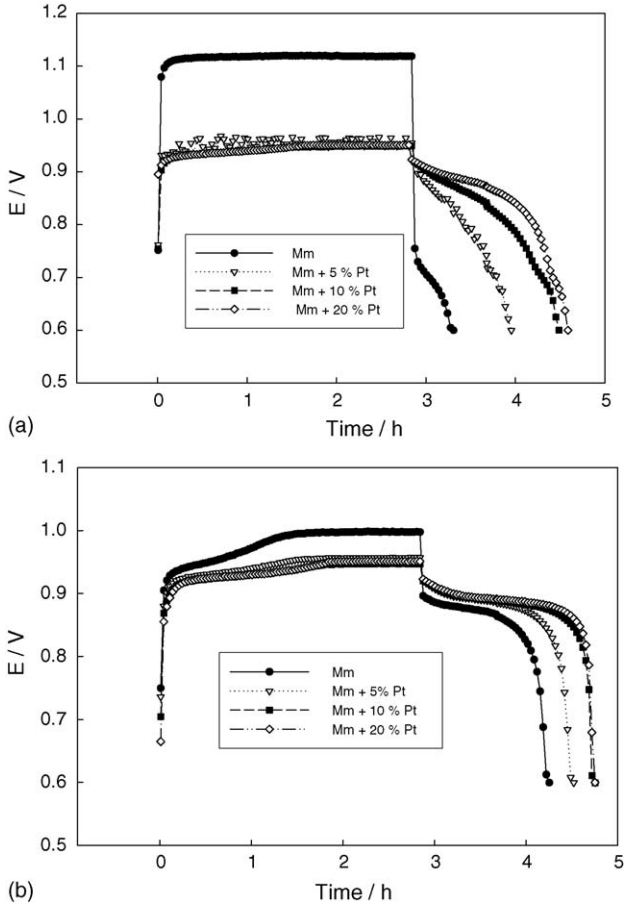

Fig. 4. Electrode potential vs. charge–discharge cycling for Pt-additivated alloy electrodes: (a) first cycle; (b) 50th cycle at C/2 rates; 7 M KOH, 23 °C.

a large ovepotential is involved between the end of charge and the beginning of the discharge; this overpotential decreases with the amount of Pt powder, which also produces an increase in the electrode capacity. As charge–discharge cycling proceeds, the charge overpotential gradually decreases and capacity increases (Fig. 4b). Otherwise, when Ni and Pd powders are used as additives a similar behaviour is observed.

The initial high charge overpotential of metal hydride electrodes may be attributed to a surface oxide film, formed during metal alloy exposure to air. Thus, when metal catalyst powders are added, the enhanced hydrogen evolution on the catalyst surface, either promotes the fast reduction of the surface oxide as a consequence of a "reducing atmosphere", or the hydrogen atoms produced during the charge process on the catalyst surface are quickly transferred to the alloy particles and absorbed through the oxide film. Hence, the global hydriding/dehydriding processes in catalyst-additivated electrodes are favored by the initial decrease in charge–discharge overpotentials, leading to higher discharge capacity values even for the first charge–discharge cycles; in turn, enhanced H entrance induces volume changes that produce pulverization of the metal particles and a subsequent decrease in diffusion overpotential during charge–discharge cycling. In this respect, it must be noted that all these processes become significant after 50 cycles for metal alloy electrodes without metal catalyst additives while less than

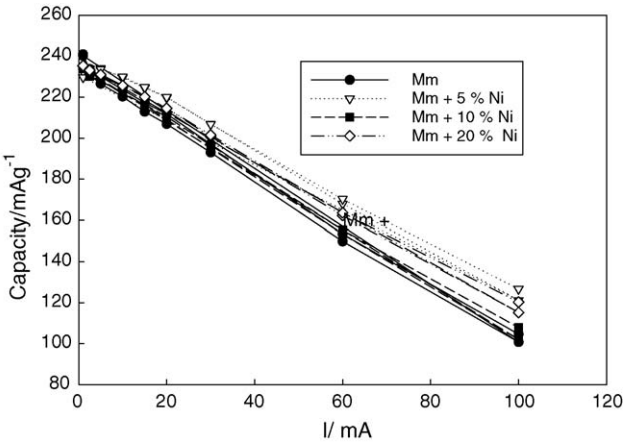

Fig. 5. Capacities of the Mm-based alloy electrodes with different Ni powder content vs. discharge currents, charge at C/2; 7 M KOH, 23 °C.

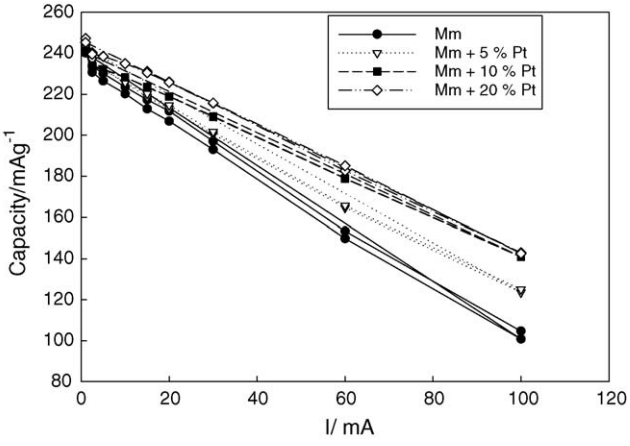

Fig. 7. Capacities of the Mm-based alloy electrodes with different Pt powder content vs. discharge currents, charge at C/2; 7 M KOH, 23 °C.

10 cycles are required for the full activation of the catalyst-additivated electrodes.

3.3. Discharge rate-capability

Fig. 5 shows the capacities of the Ni-additivated alloy electrodes at different discharge currents. It is observed that, at high discharge currents, the electrode capacity improves with Ni powder addition, being the rate-capability behaviour in accordance with the observed reduction in charge–discharge overpotentials. Fig. 6 shows the dependence of the metal alloy electrode capacity on discharge currents for different Pd contents. It is observed that both the capacity and rate-capability are improved with the increase in Pd content. The ability of Pd to form hydride compounds is responsible for higher capacity values at zero discharge current. Fig. 7 shows the rate-capability of metal alloys with different Pt content, the behaviour being similar to alloys with Ni addition. It is clear that the incorporation of metal catalysts increases the rate dischargeability of the metal hydride electrodes. In Fig. 8, capacity versus metal catalyst weight per cent plots are depicted. The capacity values in Fig. 8 correspond to the extrapolation to zero current of the plots depicted in Figs. 5–7. The linear dependence between capacity and metal catalyst percentage observed for Pd-additivated electrodes, indicates that the hydride-forming ability of Pd is responsible for the increase in capacity values at zero discharge current.

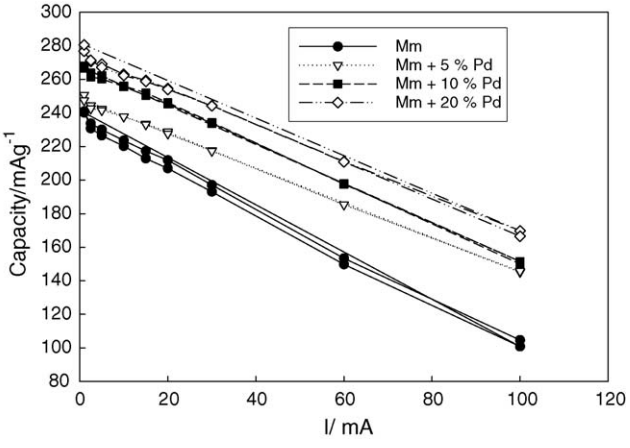

Fig. 6. Capacities of the Mm-based alloy electrodes with different Pd powder content vs. discharge currents, charge at C/2; 7 M KOH, 23 °C.

3.4. Impedance results and physicochemical model

Impedance measurements were also performed to study the effect of metal catalyst on the hydride electrode dischargeability, at equilibrium conditions. Figs. 9–11 depict impedance plots of activated electrodes (50 charge–discharge cycles) with different metal catalyst content, at a state of discharge (SOD) equal to 50%. Impedance spectra corresponding to all the electrode compositions exhibit the same general features; a high frequency capacitive arc where the phase diminishment due to the porosity

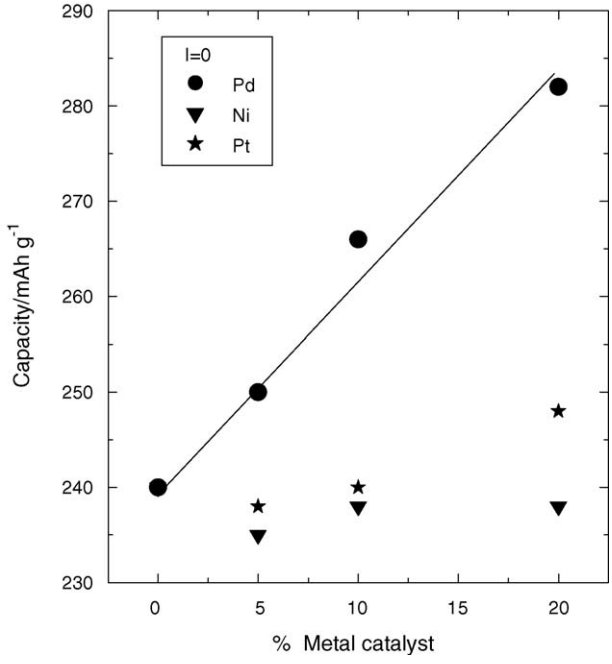

Fig. 8. Capacities at $I = 0$ of modified alloy electrodes, vs. metal catalyst weight per cent, charge at C/2; 7 M KOH, 23 °C.

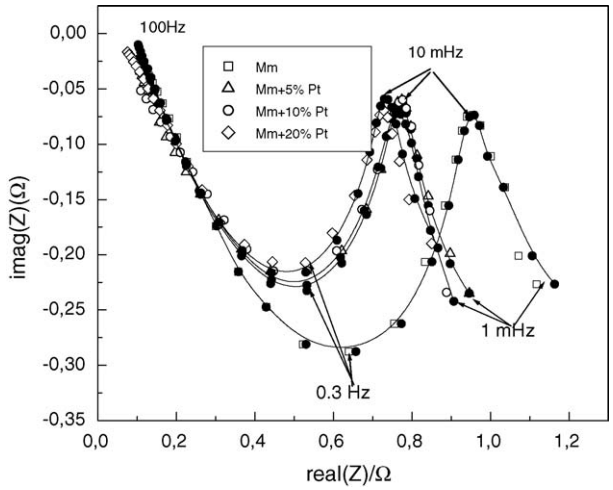

Fig. 9. Experimental and theoretical impedance spectra of Mm-based alloy electrodes with different Pt powder content, after 50 charge–discharge cycles.

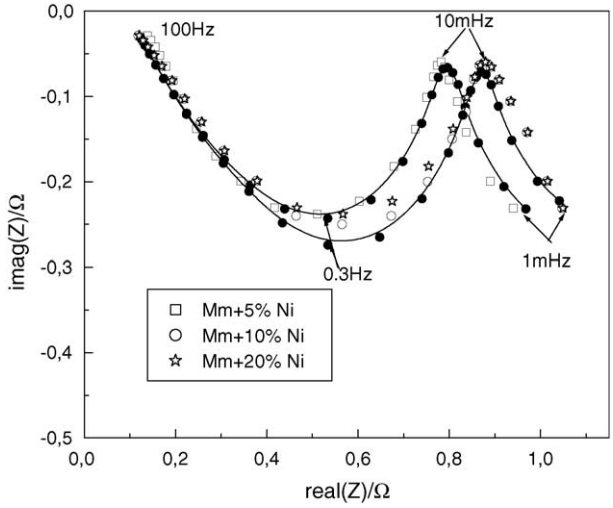

Fig. 10. Experimental and theoretical impedance spectra of Mm-based alloy electrodes with different Ni powder content, after 50 charge–discharge cycles.

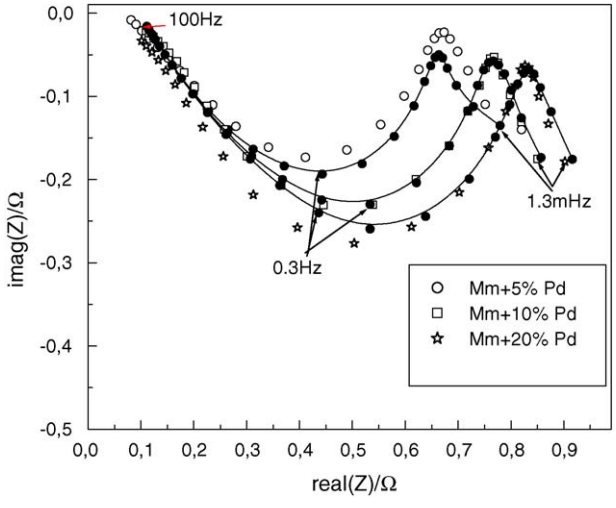

Fig. 11. Experimental and theoretical impedance spectra of Mm-based alloy electrodes, with different Pd powder content, after 50 charge–discharge cycles.

of the electrode is evident, and a low frequency region with a phase angle close to 45°, characteristic of diffusion processes. Data affected by the inductive response at very high frequencies were disregarded [27].

The theoretical impedance plots included in Figs. 9–11 were derived in terms of a physicochemical model [18] in which the porous nature of the electrode material is taken into account, considering a finite conductivity for both the solid and liquid phases. The hydrogen absorption/desorption processes, taking place at the walls of spherical alloy particles of average size, are described in terms of a kinetic scheme for hydrogen adsorption coupled to hydrogen diffusion into the electrode material. The state of discharge of the electrode is related to the boundary conditions necessary to solve the transport equations.

As a first approach the electrode is considered as a compact packing of quasi-spherical alloy particles and carbon particles. In the model an average radius r_a, is assumed for all alloy particles. Following the analysis given by De Levie [19] and Newman and co-workers [20], the impedance function of the porous structure, Zp may be expressed as:

$$Z_p = \frac{L}{\kappa + \sigma}\left[1 + \frac{2 + \left(\frac{\sigma}{\kappa} + \frac{\kappa}{\sigma}\right)\cosh \nu}{\nu \sinh \nu}\right] \quad (1)$$

where

$$\nu = L\left(\frac{\kappa + \sigma}{\kappa\sigma}\right)^{1/2} Z_i^{-1/2}$$

being, L, the electrode thickness, $L = 0.1$ cm, κ and σ, the conductivities of the liquid and solid phases, respectively, multiplied by the associated volume fraction and Z_i is the impedance of the solid/liquid interface per electrode unit volume ($\Omega\,cm^3$).

Z_i, implies the double layer capacitance impedance (Z_{dl}) linked in parallel with the Faradaic reaction impedance (Z_F), i.e.

$$Z_i^{-1} = Z_{dl}^{-1} + Z_F^{-1} \quad (2)$$

where

$$Z_{dl} = \frac{1}{i\omega C_{dl} a_e} \quad (3)$$

being, C_{dl}, the double layer capacitance per unit interfacial area ($F\,cm^{-2}$), a_e, the interfacial area per unit volume (cm^{-1}) and $\omega = 2\pi f$ (f, frequency of the perturbing signal). And

$$Z_F = \frac{Z_f}{a_a} \quad (4)$$

where Z_f is the Faradaic impedance per unit interfacial area ($\Omega\,cm^2$) and a_a is the active area per unit volume.

In the derivation of Z_f, the discharge process is described in terms of the shrinking core model [18,21–23]. At a given state of discharge, SOD, the alloy particles are considered to be constituted by two phases: the hydride core, phase β, with a uniform molar H concentration C_β, and the solid solution, α phase, with a bulk H concentration C_α. Equilibrium conditions

at the α/β interface are assumed, being the α/β interface located at:

$$r_h = \left(1 - \frac{SOD C_\beta}{C_\beta - C_\alpha}\right)^{1/3} r_a \quad (5)$$

The global dehydriding process of an alloy particle:

$$MH_x + xOH^- \rightarrow xH_2O + e^- + M$$

involves the following steps:

(a) Nucleation and growth of the α phase at the α/β interface.
(b) Diffusion of H through the α phase towards the metal/electrolyte interface.
(c) Transfer of H atoms from an interstitial site in the α phase (S), (just beneath the metal surface) to a surface site (M^s), according to the following reaction:

$$M^s + SH_{ab} \underset{k_{-1}}{\overset{k_1}{\Leftrightarrow}} MH_{ad} + S,$$

(I) H absorption/(desorption) reaction (HAR)

$$\nu_I = k_1(1-\theta)X_\alpha^s - k_{-1}\theta(1 - X_\alpha^s)$$

where k_1 and k_{-1} are potential independent specific rate constants and θ is the hydrogen adatom (H_{ad}) surface coverage.

The H molar concentration quotient in the α phase at the surface of the alloy particle (X_α^s), at $r = r_a$ (first metal monolayer), can be expressed as:

$$X_\alpha^s = C_\alpha^s / C_O$$

C_O being the molar concentration of interstitial sites available for hydrogen [18].

(d) Electrochemical oxidation of the adsorbed intermediate H_{ad}, expressed as:

$$MH_{ad} + OH^- \underset{k_{-2}}{\overset{k_2}{\Leftrightarrow}} H_2O + M^s + e^- \quad \text{(II) Volmer step}$$

$$\nu_{II} = k_2\theta - k_{-2}(1-\theta)$$

where $k_i = k_i^o \exp(b_i E)$, and $b_i = \beta_i F/RT$, $b_{-i} = -(1-\beta_i)F/RT$.

According to the high charging efficiency of these alloys, the steps related to hydrogen evolution are disregarded and the Faradaic current is given by:

$$i_F = F\nu_{II} = k_2\theta - k_{-2}(1-\theta) \quad (6)$$

Z_f may now be derived from (6):

$$\frac{1}{Z_f} = \frac{\Delta i_f(\omega)}{\Delta E(\omega)} = \left(\frac{\partial i_f}{\partial E}\right)_\theta + \left(\frac{\partial i_f}{\partial \theta}\right)_E \frac{\Delta\theta(\omega)}{\Delta E(\omega)} \quad (7)$$

Being:

$$\frac{1}{R_T} = \left(\frac{\partial i_f}{\partial E}\right)_\theta = F(k_2 b_2 \theta^{ss} - k_{-2} b_{-2}(1-\theta^{ss})) \quad (8)$$

As impedance data were recorded under equilibrium conditions, $I = 0$:

$$\frac{1}{R_T} = j_o(b_2 - b_{-2}) = j_o \frac{F}{RT} \quad (9)$$

where j_o is the exchange current density and

$$\left(\frac{\partial i_f}{\partial \theta}\right)_E = F(k_2 + k_{-2})$$

Accordingly:

$$\frac{1}{Z_f} = j_o \frac{F}{RT} + F(k_2 + k_{-2}) \frac{\Delta\theta(\omega)}{\Delta E(\omega)} \quad (10)$$

If the equilibrium of step (c) is not disturbed by the perturbing signal:

$$k_1(1-\theta)X_\alpha^s \cong k_{-1}\theta(1 - X_\alpha^s)$$

and after Taylor expansion and Fourier transform:

$$\frac{\Delta\theta(\omega)}{\Delta E(\omega)} = \frac{-\left(\frac{\partial \nu_I}{\partial X_\alpha}\right)}{\left(\frac{\partial \nu_I}{\partial \theta}\right)} \frac{\Delta X_\alpha(\omega)}{\Delta E(\omega)} \quad (11)$$

$$\frac{\Delta\theta(\omega)}{\Delta E(\omega)} = \frac{k_1(1-\theta) + k_{-1}\theta}{k_1 X_\alpha + k_{-1}(1 - X_\alpha)} \frac{\Delta X_\alpha(\omega)}{\Delta E(\omega)} \quad (12)$$

For mathematical simplification $\Delta X_\alpha(\omega)/\Delta E(\omega)$ shall be replaced by:

$$\frac{\Delta X_\alpha(\omega)}{\Delta E(\omega)} = M(\omega) \frac{\Delta J_H(\omega)}{\Delta E(\omega)} \quad (13)$$

being $M = \Delta X_\alpha / \Delta J_H$ the mass transfer function [24] and J_H the hydrogen flux at the alloy particle surface $r = r_a$.

The mass balance of the adsorbed intermediate may be written as [18]:

$$\Gamma \, d\theta/dt = J_H - \nu_{II} \quad (14)$$

where Γ corresponds to the H_{ad} maximum surface concentration. After Fourier transform of Eq. (14) and introducing Eqs. (12) and (13):

$$\Gamma j\omega \frac{\Delta\theta}{\Delta E} = \frac{\Delta J_H(\omega)}{\Delta E} - \frac{1}{F Z_f} \quad (15)$$

$$\Gamma j\omega \frac{k_1(1-\theta) + k_{-1}\theta}{k_1 X_\alpha + k_{-1}(1 - X_\alpha)} M(\omega) \frac{\Delta J_H(\omega)}{\Delta E(\omega)} = \frac{\Delta J_H(\omega)}{\Delta E(\omega)} - \frac{1}{F Z_f} \quad (16)$$

Now Z_f may be derived in terms of Eqs (10) and (16):

$$Z_f = \frac{RT}{j_o F} + \frac{RT}{j_o F}(k_2 + k_{-2})\left[\Gamma j\omega - \frac{1}{\frac{k_1(1-\theta)+k_{-1}\theta}{k_1 X_\alpha + k_{-1}(1-X\alpha)} M(\omega)}\right]^{-1} \quad (17)$$

The expression for $M(\omega)$, is derived by solving Fick's laws for radial diffusion in a spherical particle of radius r_a, being the electrochemical interface located at r_a and with the boundary condition at r_h, determined by the constant concentration X_α [24–26]:

$$M(\omega) = \frac{r_a}{C_o D} \frac{1}{\psi_a \coth(\psi_h - \psi_a) + 1} \quad (20)$$

being:

$$\psi_a = r_a\sqrt{\frac{i\omega}{D}} \qquad \psi_h = r_h\sqrt{\frac{i\omega}{D}}$$

where D is the diffusion coefficient of H in the α phase.

Using the steady-state conditions [18]:

$$\theta_{ss} = \frac{k_{-2}}{k_2 + k_{-2}} \quad (18)$$

$$X_\alpha^s = X_\alpha = \frac{k_{-1}\theta}{k_{-1}\theta + k_1(1-\theta)} \quad (19)$$

The final expression for Z_f may be derived:

$$Z_f = \frac{RT}{j_o F} + \frac{1}{\frac{F^2\Gamma j\omega(\theta(1-\theta))}{RT} - \frac{F^2 X_\alpha(1-X_\alpha)}{RTM(\theta)}} \quad (20)$$

Eq. (20) may be further simplified if: $\Gamma j\omega\theta(1-\theta) \ll X_\alpha(1-X_\alpha)/M(\omega)$:

$$Z_f = \frac{RT}{j_o F} - \frac{RTr_a}{F^2 X_\alpha(1-X_\alpha)C_o D(\psi_a \coth \psi_h - \psi_a) + 1)} \quad (21)$$

When this is the case, impedance spectra exhibit only two arcs: the arc at high frequencies corresponding to the charge transfer resistance, R_T, in parallel connection with the double layer capacitance and the arc in the lower frequency range corresponding to the impedance associated with H diffusion in the spherical alloy particles.

In order to identify the different parameters of the system, a fitting procedure of the experimental impedance data in terms of the proposed model was accomplished. A fitting program was developed, based on the Nelder-Meade simplex search algorithm [18]. The fitting was considered acceptable when, the cost function, $J_p < 5.10^{-3}$.

The corresponding theoretical plots included in Figs. 9–11, were calculated in terms of Eqs. (1) and (21), indicating a good accordance, in the whole frequency range. The parameters, derived from the fitting procedure, used in the calculation of Z_p are depicted in Tables 1 and 2.

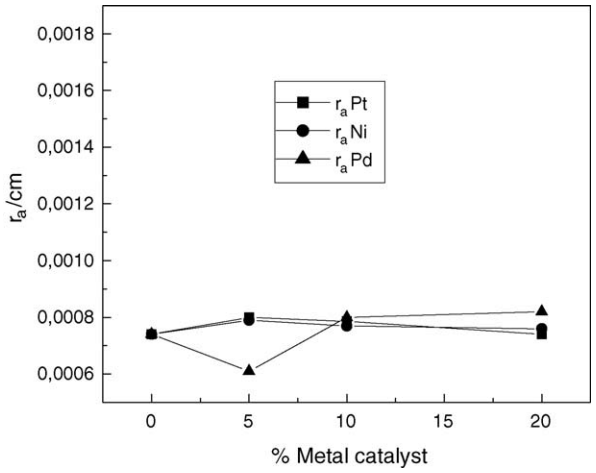

Fig. 12. Average particle radius (r_a) vs. metal catalyst weight per cent plots.

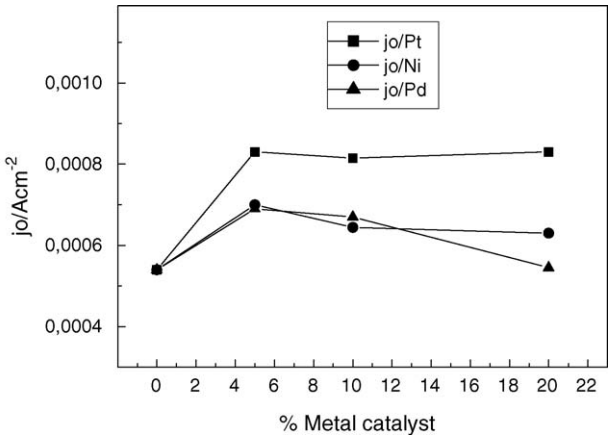

Fig. 13. Exchange current density (j_o) vs. metal catalyst weight per cent plots.

In Figs. 12–14, graphics of the parameters assembled in Table 2 as a function of the electrode composition are depicted. Fig. 12 indicates the same average particle radius, r_a, for all the activated electrodes (after 50 charge–discharge cycles) independent of the electrode composition.

In Fig. 13, the j_o versus electrode composition plots exhibit higher values of j_o, for alloy electrodes with Pt powder, as compared with alloy electrodes containing Ni and Pd powders. The higher values of j_o for Pt-additivated electrodes are in accordance with smaller charging–discharging overpotentials, as depicted in Fig. 4. As discussed in [28], the improved performance of the alloy electrodes with Ni, Pd and Pt is related to the catalytic effect of these metals on the electrochemical reactions at the alloy surface.

Table 1
Parameters from Ref. [15]

a_e (cm^{-1})	C_{dl} (F cm^{-2})	C_O (mol cm^{-3})	C_α (mol cm^{-3})	C_β (mol cm^{-3})	σ (S cm^{-1})	κ (S cm^{-1})
2.5×10^5	5×10^{-5}	0.02	[0.01–0.014]	0.06	>15	[0.15–0.17]

Table 2
Parameters derived from the fitting procedure

Electrode	a_a (cm^{-1})	j_o (A cm^{-2})	r_a (cm)	D (cm^2 s^{-1})
Mm	[700–725]	[5–5.4] × 10^{-4}	[7–7.5] × 10^{-4}	[2–4] × 10^{-10}
Mm + 5% Pt	[770–820]	[8–8.5] × 10^{-4}	[7.8–8] × 10^{-4}	[2–4] × 10^{-10}
Mm + 10% Pt	[780–820]	[7.9–8.2] × 10^{-4}	[7.8–8] × 10^{-4}	[2–4] × 10^{-10}
Mm + 20% Pt	[840–880]	[8–8.3] × 10^{-4}	[7.3–7.5] × 10^{-4}	[2–4] × 10^{-10}
Mm + 5% Ni	[780–820]	[6.9–7.2] × 10^{-4}	[7.8–8] × 10^{-4}	[2–4] × 10^{-10}
Mm + 10% Ni	[815–835]	[6.5–6.9] × 10^{-4}	[7.6–7.8] × 10^{-4}	[2–4] × 10^{-10}
Mm + 20% Ni	[700–720]	[6–6.5] × 10^{-4}	[8.8–9] × 10^{-4}	[2–4] × 10^{-10}
Mm + 5% Pd	[1100–1200]	[6.7–7] × 10^{-4}	[6–6.2] × 10^{-4}	[2–4] × 10^{-10}
Mm + 10% Pd	[900–1100]	[6.5–6.9] × 10^{-4}	[7.8–8.2] × 10^{-4}	[2–4] × 10^{-10}
Mm + 20% Pd	[900–1050]	[5–5.7] × 10^{-4}	[8–8.4] × 10^{-4}	[2–4] × 10^{-10}

Fig. 14 shows a_a versus electrode composition plots. The alloy electrodes with Pt and Ni additives exhibit approximately the same active areas than electrodes without additives. Impedance data corresponding to Pd-additivated electrodes were fitted with higher values of a_a. The higher a_a values for Pd-additivated electrodes may be attributed to the hydride-forming ability of polycrystalline Pd. It is interesting to note that a_a is directly proportional to the weight of active material and inversely proportional to the size of alloy particle. If all the alloys particles have an average radius r_a, a_a may be estimated, as a first approach, with:

$$a_a = 3m/(r_a \rho V_e) \quad (22)$$

being, $m = 0.075$ g is the alloy weight, $\rho \approx 3.6$ g cm^{-3}, the alloy density and $V_e = 0.1$ cm^3 is the electrode volume.

The comparison of a_a values between electrodes with and without Pd of the same r_a, (e.g. 10 wt.% Pd) indicates an increase in the a_a value for Pd-additivated electrodes, which may be attributed to the contribution of active area related to Pd powder. On the other hand, by comparing a_a values between Pd-additivated electrodes it must be taken into account that r_a value is $r_a \approx 6 \times 10^{-4}$ cm for 5 wt.% Pd electrodes, and $r_a \approx 8 \times 10^{-4}$ for 20 wt.% Pd. This increase in r_a (Fig. 12) produces a decrease in a_a, which compensates the increase in Pd powder weight, as depicted in Fig. 14. We think that the differences in r_a shown in Fig. 12, are due to dispersion of experimental results. The occurrence of higher a_a values for smaller r_a is an indication of the validity of the proposed model.

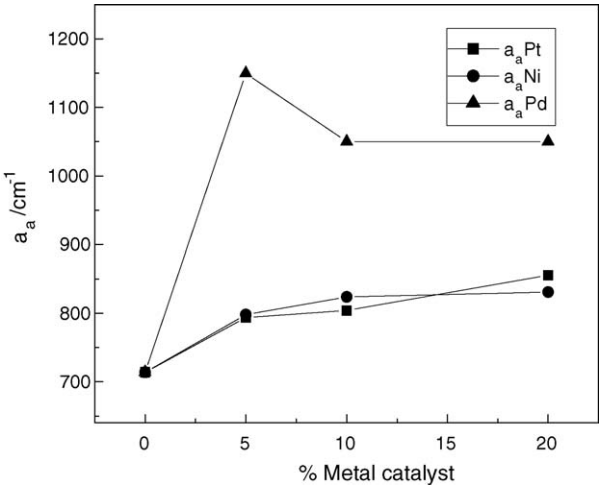

Fig. 14. Active area (a_a) vs. metal catalyst weight per cent plots.

The EIS technique was also used to investigate the cycling stability of the hydride electrodes. As depicted in Figs 1–3, there is a sharp decrease of the electrode capacity after 150 charge–discharge cycles. In Fig. 15 the impedance response of metal hydride electrodes subjected to 200 charge–discharge cycles is presented and compared with the EIS spectra of electrodes subjected to 50 cycles. As depicted in the figure, the decrease in capacity on cycling is accompanied by an increase in the impedance of the electrode at low frequencies. The impedance spectra of alloy electrodes with low additive content, exhibit the same general features as electrodes subjected to 50 charge–discharge cycles. The theoretical plots included in Fig. 14a and b, were calculated in terms of Eqs. (1) and (21), being the parameters, derived from the fitting procedure, approximately coincident with the ones assembled in Tables 1 and 2; only the active area, a_a, changes appreciably as indicated in Table 3. Electrodes with a higher content of metal catalyst additive, e.g. 20 wt.% Ni, after 200 cycles, do not exhibit an impedance response in accordance with the proposed model; accordingly, the reduction in electrode capacity after prolonged cycling seems to be due to the decrease in active area. This fact can be explained taking into account that the metal alloy lattice is subjected to continuous expansion and contraction cycles as a consequence of hydriding/dehydriding processes, which produces cracks in the alloy particles, after the electrode is fully activated. The cracks expose fresh alloy surfaces, which react easily with the electrolyte and produce oxides; this process

Table 3
Active area values corresponding to metal hydride electrodes subjected to 200 charge–discharge cycles

Electrode	a_a (cm^{-1})
Mm	[415–435]
Mm + 5%Pt	[360–386]
Mm + 10%Pt	[355–395]
Mm + 5%Ni	[150–170]
Mm + 10%Ni	[270–290]
Mm + 5%Pd	[358–385]

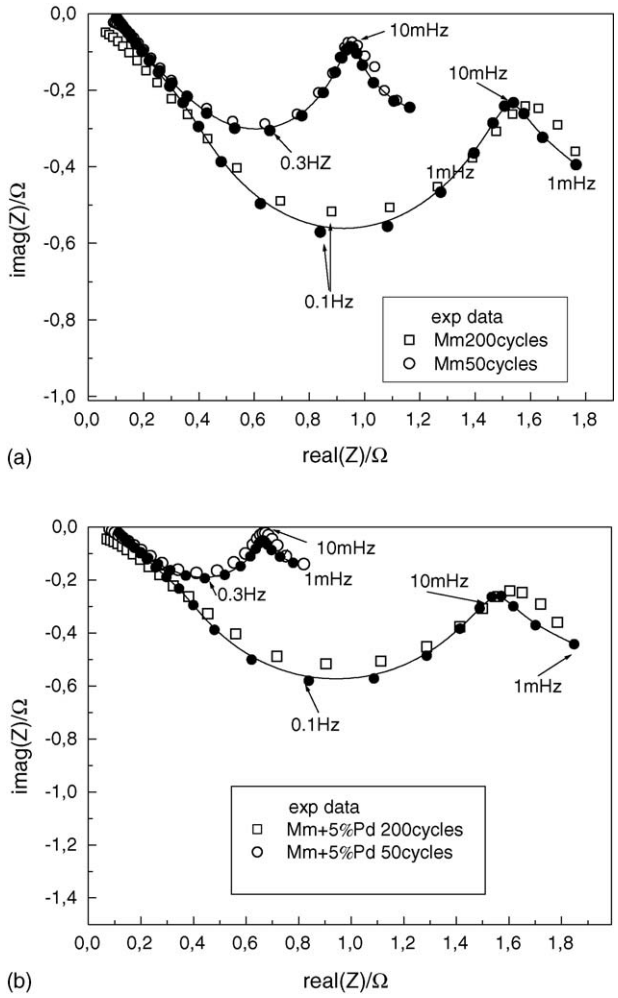

Fig. 15. Effect of the number of charge–discharge cycles on the impedance response of Mm-based electrodes, (a) without additives; (b) with 5 wt.% Pd powder.

finally leads to pulverization of the alloy particles and losses in the electrical contact among catalyst particles themselves, and between them and the current collector [29].

4. Conclusions

The addition of Ni, Pd and Pt powders to AB_5-type metal alloy electrodes, largely accelerates the activation process and enhances the rate-capability. However, the cycle stability of metal hydride electrodes is not increased. The fast activation and high rate-capability of metal alloy electrodes with Pt, Pd and Ni powder addition are attributed to the enhanced catalytic ability for hydrogen oxidation/reduction processes, which is confirmed by the overpotential curves during charge–discharge cycles and the exchange current obtained from EIS.

The identification of impedance data, in terms of the proposed model, allowed the estimation of parameters such as the exchange current density, j_o, the active area per unit volume, a_a, and the average radius of metal particles, r_a. From the identification procedure it may be concluded that the addition of the metal catalysts is capable of modifying the charge transfer reaction kinetics but not the diffusion coefficient of hydrogen in the metal alloy. EIS identification also indicates that after 50 activation cycles, all electrodes exhibit the same particle average radius. The slightly higher capacity of Pd-additivated electrode can be attributed to the fact that polycrystalline Pd is also a hydrogen-storage material. EIS analysis shows that the electrode capacity decay after prolonged charge–discharge cycling is due to the decrease in the available active area resulting from deterioration in the electrode mechanical stability, which produces losses in the electrical connection between alloy particle-to-particle and alloy particle-to-current collector.

Acknowledgments

This work was supported by Consejo Nacional de Investigaciones Científicas y Técnicas of Argentina and the Agencia Nacional de Promoción Científica y Tecnológica. The authors also thank financial support through CONICET-National Science Foundation cooperative agreement. MPS would further acknowledge additional partial support from the Welch Foundation.

References

[1] S.R. Ovshinsky, M.A. Fetcenko, J. Ross, Science 269 (1993) 176.
[2] R.C. Stempel, S.R. Ovshinsky, P.R. Gifford, D.A. Corrigan, IEEE Spectrum 35 (1998) 11.
[3] J.J.G. Willems, Philips J. Res. 39 (Suppl. 1) (1984).
[4] L.O. Valøen, Metal hydrides for rechargeable batteries, Thesis, Department of Materials Technology and Electrochemistry, Norwegian University of Science and Technology, 2000.
[5] J.-M. Joubert, M. Latroche, A. Percheron-Guégan, J. Bouet, J. Alloys Compd. 240 (1996) 219.
[6] E. Boschung, A. Züttel, D. Chartouni, L. Schlapbach, J. Alloys Compd. 274 (1998) 294.
[7] M. Bououdina, H. Enoki, E. Akiba, J. Alloys Compd. 281 (1998) 290.
[8] B.S. Chao, R.C. Young, S.R. Ovshinsky, D.A. Pawlik, B. Huang, J.S. Im, B.C. Chakoumakos, Mater. Res. Soc. Symp. Proc. 575 (2000) 193.
[9] R.C. Young, S.R. Ovshinsky, B. Huang, B.S. Chao, Y. Li, Mater. Res. Soc. Symp. Proc. 575 (2000) 187.
[10] M.V.C. Sastri, B. Viswanathan, S. Srinivasa Murthy, Metal Hydrides. Fundamentals and Applications, Springer Verlag, Berlin, 1998, p. 12.
[11] A. Anani, A. Visintin, K. Petrov, S. Srinivasan, J. Reilly, J. Johnson, R. Schwarz, P. Desch, J. Power Sources 47 (1994) 261.
[12] A. Visintin, H.A. Peretti, C. Tori, J.C. Bolcich, W.E. Triaca, Hydrogen Energy Progress XII 2 (1998) 1193.
[13] A. Visintin, H.A. Peretti, C.A. Tori, W.E. Triaca, Int. J. Hydrogen Energy 26 (2001) 683.
[14] J.O. Zerbino, A. Visintin, W.E. Triaca, J. Solid State Electrochem. 9 (2005) 254.
[15] A. Visintin, C.A. Tori, G. Garaventta, W.E. Triaca, J. Electrochem. Soc. 145 (1998) 4169.
[16] D.R. Barsellini, A. Visintin, W.E. Triaca, M.P. Soriaga, J. Power Sources 124 (2003) 309.
[17] D.R. Barsellini, A. Visintin, W.E. Triaca, J. Argent. Chem. Soc. 9 (2003) 183.
[18] E.B. Castro, S.G. Real, A. Bonesi, A. Visintin, W.E. Triaca, Electrochim. Acta 49 (2004) 3879.
[19] R. De Levie, in: P. Delahay (Ed.), Advances in Electrochemistry and Electrochemistry Engineering, vol. 6, Interscience, NY, 1967, p. 329.
[20] J.P. Meyers, M. Doyle, R.M. Darling, J. Newman, J. Electrochem. Soc. 147 (2000) 2930.

[21] V.R. Subramanian, H.J. Ploehn, R.E. White, J. Electrochem. Soc. 147 (2000) 2868.
[22] W. Zhang, S. Srinivasan, H.J. Ploehn, J. Electrochem. Soc. 143 (1996) 4039.
[23] C.S. Wang, Y.Q. Lei, Q.D. Wang, Electrochim. Acta 43 (1998) 3193.
[24] J.-P. Diard, B. Le Gorrec, C. Montella, J. Electroanal. Chem. 471 (1999) 126.
[25] T. Jacobson, K. West, Electrochim. Acta 40 (1995) 255.
[26] R.H. Milocco, E.B. Castro, J. Electroanal. Chem. 579 (1) (2005) 113.
[27] A. Lundqvist, G. Lindbergh, Electrochim. Acta 44 (1999) 2523.
[28] C. Wang, A.J. Appleby, F.E. Little, J. Electrochem. Soc. 148 (2001) A762.
[29] J. Nan, Y. Yang, J. You, Z. Lin, J. Power Sources 79 (1999) 64.